

Article

Porphyrin-Based Metal–Organic Frameworks for Efficient Electrochemiluminescent Chiral Recognition of Tyrosine Enantiomers

Wen-Rong Cai ^{1,2}, Wen-Kai Zhu ¹, Bao-Zhu Yang ¹, Da-Tong Wu ¹, Jun-Yao Li ¹, Zheng-Zhi Yin ^{3,*}
and Yong Kong ^{1,*}

¹ Jiangsu Key Laboratory of Advanced Materials and Technology, School of Petrochemical Engineering, Changzhou University, Changzhou 213164, China

² Shandong Key Laboratory of Biochemical Analysis, College of Chemistry and Molecular Engineering, Qingdao University of Science and Technology, Qingdao 266042, China

³ College of Chemical Sciences and Engineering, Jiaxing University, Jiaxing 314001, China

* Correspondence: yinzhengzhi@zjxu.edu.cn (Z.-Z.Y.); yzkongyong@cczu.edu.cn (Y.K.)

Abstract: Science the biological activities of chiral enantiomers are often different or even opposite, their chiral recognition is of great significance. A new assembly structure named TCPP-Zn-(S)-BINOL was obtained based on the interaction between chiral binaphthol (BINOL) and the porphyrin-based MOF structure formed by Meso-Tetra(4-carboxyphenyl)porphine (TCPP) and Zn²⁺, and a new chiral sensor was designed relying on TCPP-Zn-(S)-BINOL. The chiral platform was designed by using binaphthol as a chiral recognizer and the porphyrin MOF as an emitter, which can recognize tyrosine (Tyr) enantiomers via the electrochemiluminescence (ECL) method. According to density functional theory (DFT), TCPP-Zn-(S)-BINOL has a different affinity with L/D-Tyr due to the different strength of the hydrogen bond between chiral ligand BINOL and the tyrosine (Tyr) enantiomer. It will be more suitable for combination with L-Tyr, and the presence of L-Tyr will increase the ECL intensity of the modified electrode via the catalytic reduction of co-reactant reagents, achieving the purpose of the chiral recognition of Tyr enantiomers. These findings show that TCPP-Zn-(S)-BINOL can be used as an advanced ECL chiral recognition platform for biomedical applications.

Keywords: chiral recognition; electrochemiluminescence; meso-tetra(4-carboxyphenyl)porphine; metal–organic framework



Citation: Cai, W.-R.; Zhu, W.-K.; Yang, B.-Z.; Wu, D.-T.; Li, J.-Y.; Yin, Z.-Z.; Kong, Y. Porphyrin-Based Metal–Organic Frameworks for Efficient Electrochemiluminescent Chiral Recognition of Tyrosine Enantiomers. *Chemosensors* **2022**, *10*, 519. <https://doi.org/10.3390/chemosensors10120519>

Academic Editor: Marco Frasconi

Received: 7 November 2022

Accepted: 6 December 2022

Published: 7 December 2022

Publisher's Note: MDPI stays neutral with regard to jurisdictional claims in published maps and institutional affiliations.



Copyright: © 2022 by the authors. Licensee MDPI, Basel, Switzerland. This article is an open access article distributed under the terms and conditions of the Creative Commons Attribution (CC BY) license (<https://creativecommons.org/licenses/by/4.0/>).

1. Introduction

Chirality assumes a significant role in nature. As a key compound property of life, most organically dynamic substances have chiral characteristics, and many biological mechanisms have explicit connections with chiral molecules. Because of the precise orientation of functional groups in chiral molecules, chiral recognition likewise assumes a critical role in the fields of chemical, biological, and pharmaceutical sciences [1]. The two enantiomers of chiral molecules have similar physical and chemical properties but may have distinct roles in biological interactions, pharmacological activities, and metabolic behaviors [2,3]. In general, only one enantiomer can effectively treat diseases and show the required characteristics in the process of chiral recognition, while others might be insufficient or cause serious side effects, or even harmful impacts [4,5]. Therefore, chiral recognition is of great significance in clinical and pharmaceutical applications. Amino acids are the molecular structural units of life, which assume an essential role in many related fields, such as living systems. They are the most significant and primary chiral compounds in nature and can be utilized as significant biomarkers for different metabolic diseases [6]. For example, L-tyrosine (L-Tyr) significantly affects hyperthyroidism and can likewise prevent vitiligo. Different from L-Tyr, D-tyrosine (D-Tyr) may have a certain inhibitory effect on the body's

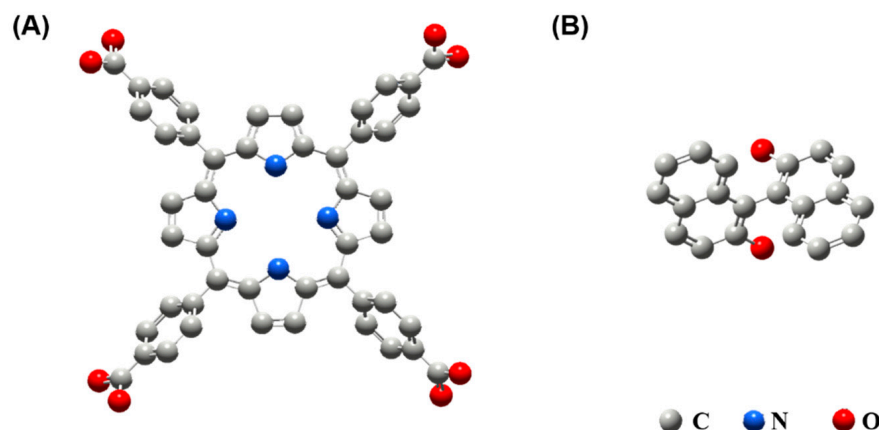
nutritional balance. Thus, developing an effective and sensitive strategy for the chiral recognition of amino acid enantiomers has important theoretical and practical significance.

At present, the identification strategies of amino acid enantiomers include high-performance liquid chromatography (HPLC) [7,8], fluorescence spectroscopy [9,10], mass spectrometry [11,12], colorimetry [13,14], capillary electrophoresis [15], Raman spectroscopy [16–18], and other technologies. Even though chromatography has a decent separation impact, the equipment and consumables are expensive and time-consuming. The pretreatment of samples by fluorescence spectrometry is generally complex, and the recognition scope of the color detection method is relatively narrow. Compared with conventional strategies, electrochemical chiral detection has the advantages of simple preparation, rapid detection, low price, real-time operation, and online analysis, and has become an important development direction in the field of chiral recognition and detection [19]. Among them, electrochemiluminescence (ECL) chiral sensors have the advantages of both electrochemistry and chemiluminescence. ECL chiral sensors have the advantages of a low background signal, good controllability, and high sensitivity, and they have drawn increasingly more attention than other methods [20,21]. There are few reports on the identification of chiral compounds by ECL methods. The development of efficient and chemically stable chiral ECL emitters and the construction of chiral sensing interfaces are considered as some of the most challenging tasks in ECL chiral sensing.

Porphyrins and their derivatives have exceptional electronic structures and photoelectric properties [22], and are widely used as cathode-efficient organic ECL emitters. In order to construct a porphyrin-based ECL chiral sensor with efficient recognition ability for amino acid enantiomers, it is necessary to impart chirality to achiral porphyrins. For achiral substances, the chiral information of chiral molecules can be transferred to the assembled aggregates of achiral molecules through weak intermolecular interactions. Generally speaking, the selected achiral substances often have multifunctional and adjustable molecular components. In this respect, porphyrin is unmatched by any other system. Porphyrins and their derivatives have a unique large p -conjugated system, and various functional groups at the ends endow porphyrins with good coordination, which can form zero-dimensional, one-dimensional, two-dimensional, or three-dimensional crystal materials in space, which is beneficial for the expression of chiral information on aggregates. The most mature method to realize the chiral assembly of porphyrins is to covalently attach the chiral part to porphyrins [23,24]. For example, Donato Monti [25] assembled porphyrins with L or D-proline tert-butyl esters to construct chiral superstructures. In addition to the modification of porphyrins with chiral functional groups, various types of chiral porphyrins have been designed. Meijer et al. [26] systematically studied the path complexity of the polymerization of chiral amide-functionalized zinc porphyrins. The hydrogen bonding of the amide part and the π - π stacking of the porphyrin backbone are the reasons for the formation of supramolecular polymers. The manipulation of the noncovalent interaction of porphyrin-based chiral supramolecular polymers leads to the responsive transition between various thermodynamically stable aggregates.

Through previous studies, it was found that assembling porphyrins into MOF structures can greatly improve the optoelectronic properties of porphyrins, and researchers have successfully prepared a series of porphyrin-based MOF structures. Based on previous research, in this work, the fabrication of a porphyrin-based ECL chiral sensor is reported for the recognition of tyrosine enantiomers. S-Binaphthol ((S)-BINOL) was selected as the chirality source and introduced into the porphyrin MOF structure constructed by Meso-Tetra(4-carboxyphenyl)porphine (TCPP) and zinc acetate, which endowed the porphyrin-assembled structure with chirality. The chemical structures of TCPP and (S)-BINOL are shown in Scheme 1. The prepared nanoscale TCPP-Zn-(S)-BINOL simultaneously inherits the feature of binaphthol as a chiral recognition center and the excellent ECL activity of porphyrin. Meanwhile, the prepared MOF structure greatly enhances the ECL intensity of porphyrin. Under optimal conditions, TCPP-Zn-(S)-BINOL has different binding abilities to L-Tyr and D-Tyr, resulting in different changes in ECL intensities, which endow the

constructed sensing interface with chiral recognition of the Tyr enantiomers. The proposed ECL chiral sensor has high stability and good repeatability, which provides a reference for the construction of a new chiral recognition and chiral sensing platform.



Scheme 1. Chemical structures of (A) TCPP and (B) (S)-BINOL.

2. Materials and Methods

2.1. Reagents and Materials

(S)-(-)-1,1'-Bi-2-naphthol ((S)-BINOL), sodium dodecyl sulfate (SDS), zinc acetate dihydrate, L-tyrosine (L-Tyr), D-tyrosine (D-Tyr), and N-(2-hydroxyethyl) piperazine-N'-(2-ethane sulfonic acid) (HEPES) sodium salt were purchased from Aladdin Chemistry Co., Ltd. (Shanghai, China). Meso-Tetra(4-carboxyphenyl)porphine (TCPP) was obtained from Macklin Biochemical Technology Co., Ltd. (Shanghai, China). All other chemicals were of analytical grade. Throughout the work, all aqueous solutions were prepared with ultrapure water (18.2 MΩ cm, Millipore, Darmstadt, Germany).

2.2. Measurement Characterization

ECL signals were recorded by an MPI-EII electrochemiluminescence analytical system (Xi'an Remex Analytical Instrument Co., Ltd., Xi'an, China). An FS5 fluorescence spectrometer (Edinburgh Instruments, Edinburgh, UK) was employed for the fluorescence spectra. Fourier transform infrared (FT-IR) spectra and ultraviolet absorption spectra were captured by a Nicolet FTIR-8400S spectrophotometer (Shimadzu, Japan) and a model U-3900 UV-vis spectrophotometer (Hitachi, Tokyo, Japan), respectively. X-ray photoelectron spectroscopy (XPS) was performed using an ESCALAB 250Xi spectrometer (ThermoFisher Scientific, Waltham, MA, USA). A Supra55 field emission scanning electron microscope (FESEM, Zeiss, Oberkochen, Germany) was used to characterize the morphologies and perform the energy-dispersive spectroscopy (EDS) of different structures. The size distribution was obtained by using a ZEN3600 laser particle size analyzer (Malvern, Worcestershire, UK). A CHI-660d electrochemical workstation was used to carry out relevant electrochemical experiments with the traditional three-electrode system—that is, a glassy carbon electrode (GCE) or modified GCE was used as the working electrode, a saturated calomel electrode (SCE) was used as the reference electrode, and platinum foil (10 × 5 mm) was the auxiliary electrode. In the electrochemical experiments, the GCEs (Φ= 5 mm) were pretreated by polishing with 0.3 and 0.05 μm alumina powders, respectively, and then the electrode was ultrasonically treated with acetone, ethanol, and double-distilled water to achieve mirror polishing. The Gaussian 09 software package was used for the molecular dynamics (MD) simulation.

2.3. Synthesis of TCPP-Zn-(S)-BINOL

TCPP-Zn-(S)-BINOL was synthesized according to the following protocol. Using 0.05 M SDS solution as the solubilizer, 1 mM TCPP, 2 mM (S)-BINOL, and 3 mM Zn(OAc)₂

solutions were prepared, respectively. Then, 5 mL of (S)-BINOL and 1 mL of $\text{Zn}(\text{OAc})_2$ were added dropwise to 4 mL of TCPP solution and stirred continuously for 12 h. The resulting nanostructure was collected by centrifugation at 11,000 rpm, and finally vacuum-dried in an oven at 60 °C to obtain TCPP-Zn-(S)-BINOL.

2.4. Electrode Preparation and Modification

First, 1.0 mg TCPP-Zn-(S)-BINOL was dispersed in 1 mL of ultrapure water and ultrasonically dispersed for 5 min. Then, 10 μL of the dispersed TCPP-Zn-(S)-BINOL solution was used to coat the surface of the GCE and dried under an infrared lamp. To improve the stability of the electrode, 10 μL of TOAB solution, which was prepared by ultrasonically dispersing 10 mmol TOAB in 1 mL of ethanol, was coated on the electrode surface. The final prepared, modified electrode was denoted TCPP-Zn-(S)-BINOL/GCE.

2.5. ECL Chiral Recognition of Tyrosine (Tyr) Enantiomers

The emission window of ECL measurements lays above the photomultiplier tube biased at 800 V. The scan rate of the ECL measurement was 50 mV s^{-1} and the scan range was from 0.0 to -1.5 V (vs. Ag/AgCl). The entire ECL was tested in 10 mM HEPES aqueous solution (pH = 8.5) with 12 mM H_2O_2 working as a co-reactant. Chiral discrimination of Tyr enantiomers was achieved by comparing the ECL intensities of TCPP-Zn-(S)-BINOL/GCE before and after the addition of 2 mM L-Tyr and D-Tyr.

3. Results and Discussion

3.1. Characterization of TCPP-Zn-(S)-BINOL

In this study, the micellar structure formed by the surfactant SDS was used as a micro-reaction site, and the hydrophobic TCPP, which worked as an ECL emitter, entered the micellar structure and coordinated with zinc ions to form a porphyrin-based MOF with an open structure. Meanwhile, the introduction of chiral (S)-BINOL imparted chirality to the porphyrin-based MOF structure. The morphology of the prepared TCPP-Zn-(S)-BINOL was characterized by SEM. As shown in Figure 1A, TCPP monomers exhibited a micron-scale random bulky structure. Nevertheless, TCPP-Zn-(S)-BINOL (Figure 1B) presented a large agglomerated structure, in which some nanoscale microspheres were embedded. The nanospheres had a uniform size distribution at approximately 450 nm in diameter, which was attributed to the uniform micelle structure provided by the SDS solution. Dynamic light scattering (DLS) results are shown in Figure 2. The size distribution of TCPP-Zn-(S)-BINOL ranged from 342 nm to 712 nm, and the average size was around 531 nm. It is worth noting that the size obtained from DLS was slightly larger than the size of nanospheres observed by SEM, which may have been caused by the residual SDS. SEM-EDS measurements were also performed on the surface of TCPP-Zn-(S)-BINOL (Figure 1C), for which the dispersion mapping of C, N, and Zn elements is shown in Figure 1D–F. The almost uniform distribution of Zn supports the successful combination of TCPP and Zn^{2+} .

In addition, the surface C 1s, O 1s, N 1s, and Zn 2p elements of TCPP-Zn-(S)-BINOL were further studied by XPS. The peaks at 284.9 eV, 286.1 eV, 286.7 eV, and 288.6 eV, shown in the C1s XPS spectrum (Figure 3A), are contributed by C–C SP^2 , C=N, C–N, and $\pi-\pi^*$ [27]. In the porphyrin monomer, the N1s XPS spectrum showed two signals, which were assigned to the imidic and pyrrolic nitrogens, respectively. Meanwhile, in TCPP-Zn-(S)-BINOL, as shown in Figure 3B, after metallization, a Zn-N peak at 402.4 eV was detected. From the surface O 1s element of TCPP (Figure 3C, image a), it can be seen that the peak centered at 532.0 eV can be attributed to the C=O bond, while the peak of 533.4 eV is related to the C–OH group [28]. After the reaction of Zn with TCPP, the peak intensity at 533.6 eV was significantly reduced (Figure 3A, image b), indicating that the carboxyl groups in TCPP were successfully coordinated with Zn^{2+} . The XPS spectrum in Figure 3D also clearly shows the Zn 2p_{3/2} and Zn 2p_{1/2} compositions at 1021.9 and 1045 eV. The results of XPS spectra further proved that Zn was successfully coordinated with TCPP and verified the successful preparation of the porphyrin-based MOF.

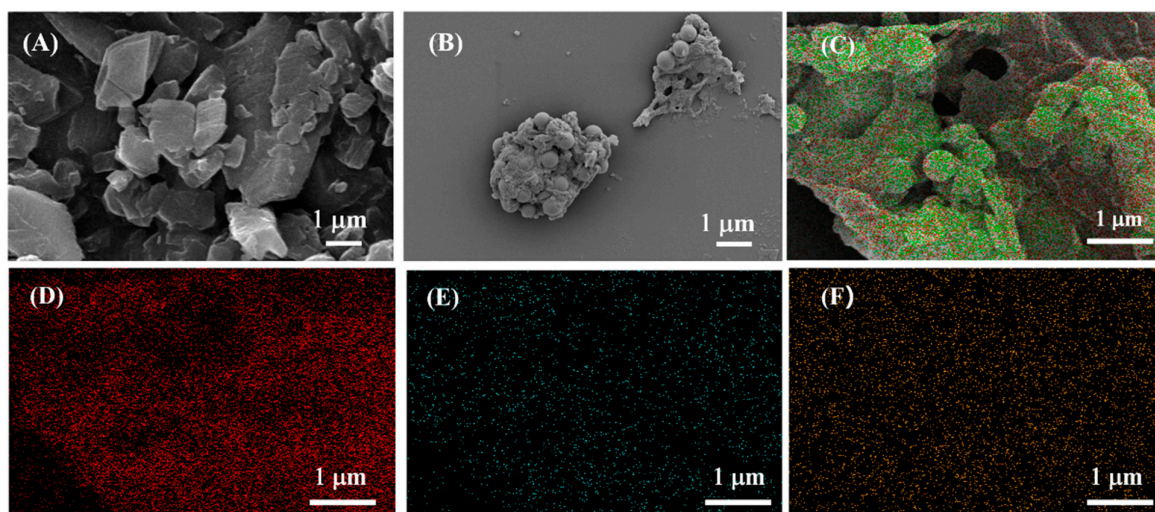


Figure 1. SEM images of (A) TCPP, (B) TCPP-Zn-(S)-BINOL. (C–F) EDS mapping image of TCPP-Zn-(S)-BINOL.

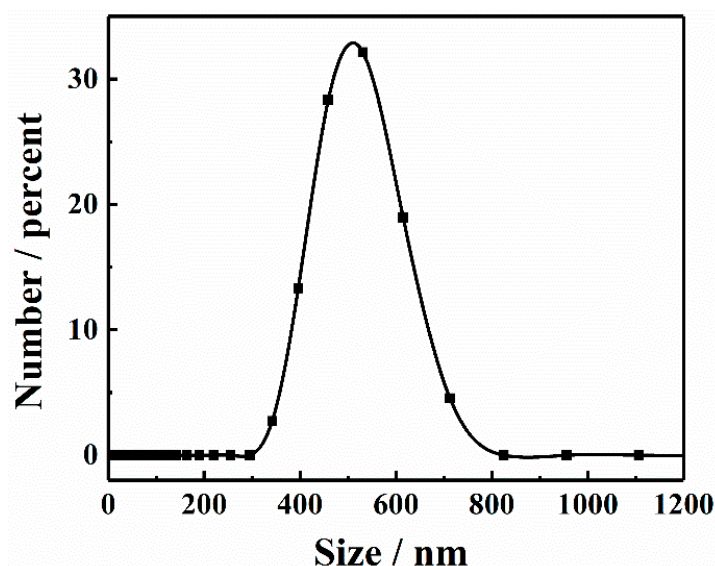


Figure 2. Size distribution of TCPP-Zn-(S)-BINOL obtained by DLS.

The formation of the Zn-TCPP MOF was further confirmed by UV–vis absorption spectroscopy. As can be seen from Figure 4A, the UV–vis spectrum of the TCPP monomer has strong Soret absorption at 416 nm, with four weak Q-bands at 512, 547, 590, and 647 nm (Figure 4A, curve a), which is dominated by the $\pi-\pi^*$ transition between the highest occupied molecular orbital (HOMO) and the lowest unoccupied molecular orbital (LUMO) [29]. In an aqueous solution, (S)-BINOL has strong absorption at 228 nm (Figure 4A, curve b). Compared with TCPP, the Soret absorption of TCPP-Zn-(S)-BINOL is red-shifted to 423 nm, corresponding to the $S_0 \rightarrow S_2$ transition (Figure 4A, curve c). In addition, the number of Q-bands was reduced to two and they were finally located at 557 and 600 nm, which was attributed to the metallation of the porphyrin [30], indicating that the center of the porphyrin was filled with metal atoms. Since both the TCPP monomer and binaphthol have absorption at 228 nm, the existence of binaphthol cannot be proven by the absorption of TCPP-Zn-(S)-BINOL at 229 nm.

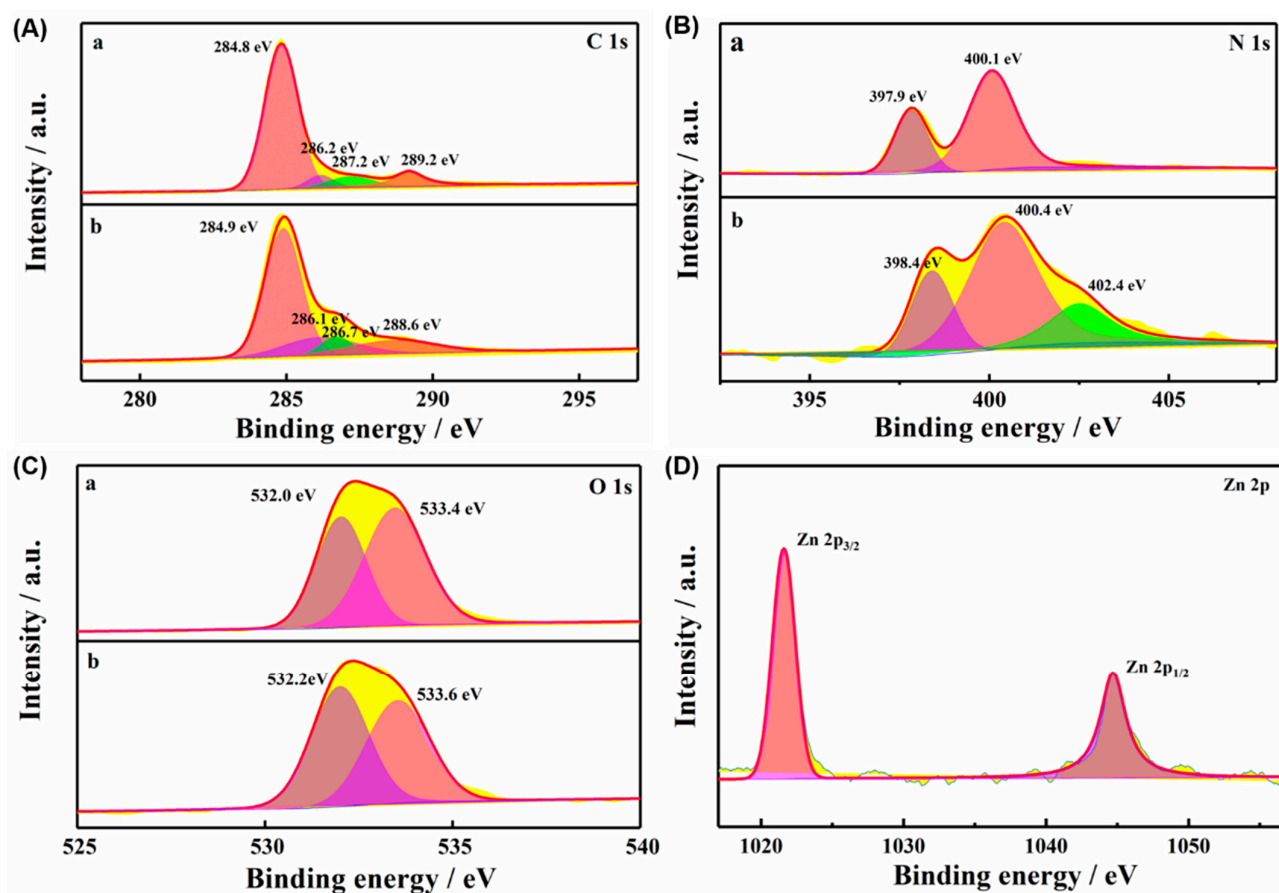


Figure 3. The high-resolution XPS response of (A) C 1s, (B) N 1s, (C) O 1s, and (D) Zn 2p of TCPP (a) and TCPP-Zn-(S)-BINOL (b).

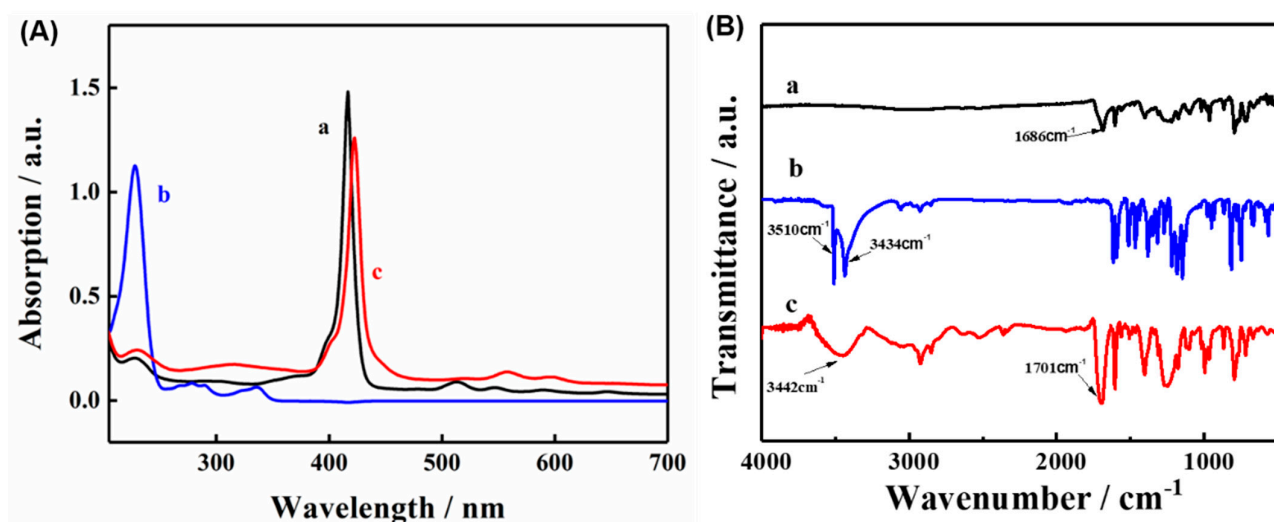
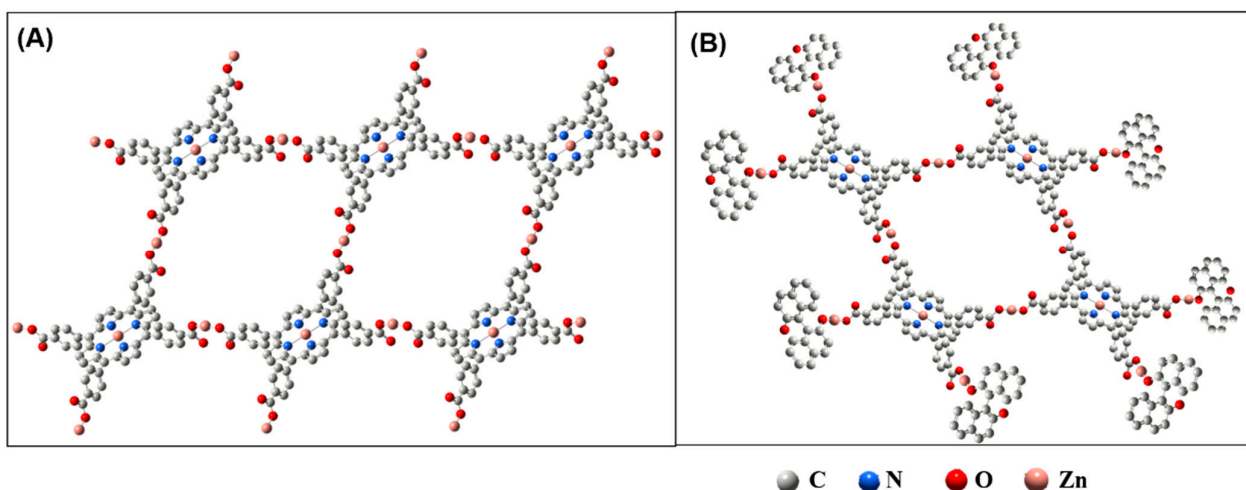


Figure 4. (A) UV-vis absorption and (B) FTIR spectra of TCPP (a), (S)-BINOL (b), and TCPP-Zn-(S)-BINOL (c).

In order to further confirm whether (S)-BINOL was successfully introduced, the FT-IR spectra of TCPP-Zn-(S)-BINOL were studied. The FT-IR spectrum of TCPP (Figure 4B, curve a) represents various characteristic bands, as reported in the literature; the typical peak is the stretching band of C=O in the carboxy group at 1686 cm⁻¹ [31]. In the FT-IR spectrum of (S)-BINOL (Figure 4B, curve b), the strong peaks at 3510 cm⁻¹ and 3434 cm⁻¹ are

assigned to the stretching vibration peaks of two phenol hydroxyl groups [32]. This is consistent with the literature reports. FT-IR of TCPP-Zn-(S)-BINOL (Figure 4B, curve c) shows the presence of both TCPP and (S)-BINOL, implying its successful formation. Among them, the stretching vibration peak of C=O has a blue shift and is finally located at 1701 cm^{-1} , which may be caused by the coordination between Zn and the carboxyl group of TCPP. The results of the FT-IR spectrum verified the successful introduction of binaphthol, indicating that the chiral source was successfully assembled into the porphyrin-based MOF structure.

According to the aforementioned experimental results and the reported literature on porphyrin-based MOFs [33,34], the structure of TCPP-Zn-(S)-BINOL was inferred. According to the literature, TCPP molecules can be linked to each other through the coordination of zinc ions and carboxyl groups to form 2D layered sheets (Scheme 2A). At the same time, the center of TCPP is metalized by Zn^{2+} ions through the Zn-N bond. The layered sheets are further stacked in the form of dislocations, and, finally, the 3D MOF structure is formed, named TCPP-Zn. The introduced chiral ligands have hydroxyl groups and can compete with TCPP to occupy the coordination orbit of metal ions. After adding BINOL, BINOL competes with TCPP and combines with zinc atoms at the edge of the grid to finally form porphyrin-based MOF structure TCPP-Zn-(S)-BINOL, as shown in Scheme 2B.



Scheme 2. Schematic illustrations for the structure of (A) TCPP-Zn and (B) TCPP-Zn-BPS.

3.2. Optimization of Experimental Conditions

The experimental conditions, including pH and sample loading, were optimized as they affected the ECL intensity of the electrode. In order to determine the optimal pH value of the reaction solution, electrolytes with different pH values were first prepared, and the ECL properties of TCPP-Zn-(S)-BINOL/GCE were tested under the same experimental conditions. It can be seen from Figure 5A that the ECL intensity of TCPP-Zn-(S)-BINOL/GCE first increases with the increase in pH value. When the pH value of the electrolyte is 8, the ECL intensity reaches the maximum value. Subsequently, with the increase in pH value, the ECL intensity decreases. This may be because the material is unstable under the condition of being too acidic or too alkaline, resulting in the reduction in ECL to varying degrees. Therefore, pH 8.0 is the most suitable for optimum ECL measurement.

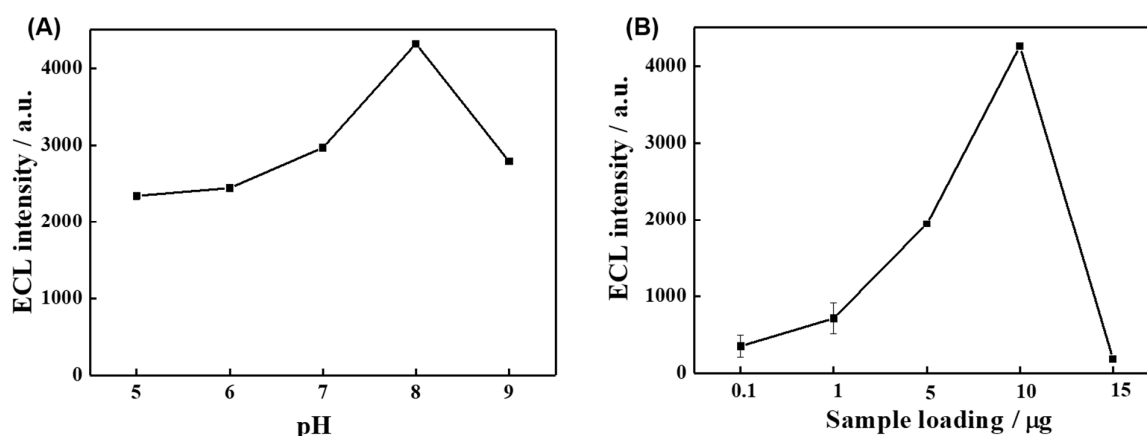


Figure 5. The optimization of ECL experimental parameters. (A) Effect of the pH. (B) The influence of the weight of sample loading.

Furthermore, the sample loading of the modified electrode was optimized. It can be seen from Figure 5B that the optimal sample loading is 10 μg . Initially, with the increase in sample loading, the ECL intensity of the electrode was gradually enhanced. However, due to the poor electron transport capability of TCPP-Zn-(S)-BINOL, loading excess sample would affect the electrochemical activity of TCPP-Zn-(S)-BINOL/GCE, which affects its ECL performance in turn. Therefore, the sample loading of 10 μg was chosen for subsequent experiments.

3.3. ECL Behavior and Mechanism of TCPP-Zn-(S)-BINOL

Under the optimized conditions, the ECL performance of different electrodes was tested in 10 mM HEPES (pH = 8.0) electrolyte in the presence of 12 mM H_2O_2 with a sample loading of 10 μg . As shown in Figure 5A, the TCPP (Figure 6A, curve a) and (S)-BINOL (Figure 6A, curve b) monomers have no obvious ECL signal, while a strong ECL signal with the intensity of 4300 a.u. was observed for TCPP-Zn-(S)-BINOL/GCE and an ECL peak of TCPP-Zn-(S)-BINOL/GCE appeared at the potential of -1.38 V. The relative standard deviation (R.S.D.) was 1.15% for eight successive scans, indicating the great stability of TCPP-Zn-(S)-BINOL/GCE (Figure 6B).

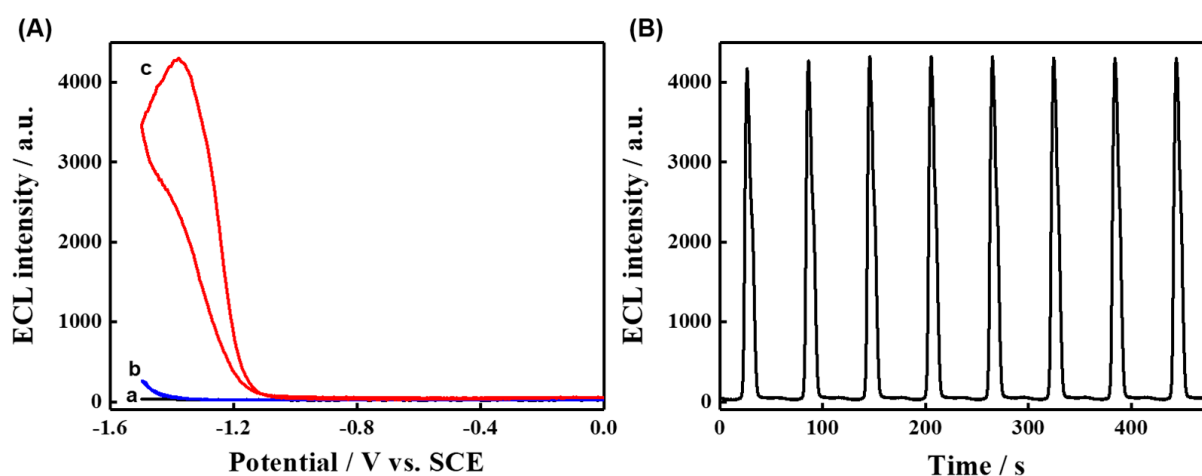


Figure 6. (A) ECL potential curves of TCPP (a), (S)-BINOL (b), and TCPP-Zn-(S)-BINOL (c). (B) ECL behaviors of TCPP-Zn-(S)-BINOL/GCE during a continuous potential scan between -1.5 and 0.0 V.

In order to explore the enhanced ECL mechanism of TCPP-Zn-(S)-BINOL, the electrochemical properties of different modified electrodes were investigated. Electrochemistry is an effective means to reflect the electrocatalytic activity of modified electrodes. As shown in

Figure 7, the CVs of TCPP, (S)-BINOL, and TCPP-Zn-(S)-BINOL at a scan rate of 50 mM s^{-1} and scanning potential from 0 to -1.5 V were measured in 10 mmol L^{-1} HEPES buffer with or without H_2O_2 . TCPP/GCE (Figure 7A, curve a) has two obvious reduction peaks at -0.53 V and -0.92 V , and two weak reduction peaks at -1.19 V and -1.35 V , respectively, corresponding to the four-step electron loss progress of porphyrin, which is consistent with the literature reports [35]. (S)-BINOL/GCE (Figure 7B, curve a) has no obvious redox peak, and the -0.58 V peak is attributed to the reduction peak of oxygen. The reduction peaks of TCPP-Zn-(S)-BINOL/GCE (Figure 7C, curve a) are slightly shifted relative to TCPP and finally located at -0.53 V , -0.90 V , -1.09 V , and -1.30 V , corresponding to $\text{TCPP-Zn}^{2+}\text{-(S)-BINOL} \rightarrow \text{TCPP-Zn}^{\bullet+}\text{-(S)-BINOL} \rightarrow \text{TCPP-Zn}^0\text{-(S)-BINOL} \rightarrow \text{TCPP}^{\bullet-}\text{-Zn}^0\text{-(S)-BINOL} \rightarrow \text{TCPP}^{2-}\text{-Zn}^0\text{-(S)-BINOL}$ [36]. In the presence of H_2O_2 , both TCPP/GCE (Figure 7A, curve b) and (S)-BINOL/GCE (Figure 7B, curve b) showed a catalytic reduction ability, while the electrochemical current of TCPP-Zn-(S)-BINOL/GCE (Figure 7C, curve b) increased significantly, in which $\text{TCPP}^{\bullet-}\text{-Zn}^0\text{-(S)-BINOL}/\text{TCPP}^{2-}\text{-Zn}^0\text{-(S)-BINOL}$ had the most obvious effect on the catalytic reduction of H_2O_2 , indicating that it has a good catalytic effect on H_2O_2 and can generate a large number of $\bullet\text{OH}$, which is a key substance in the luminescence process of ECL.

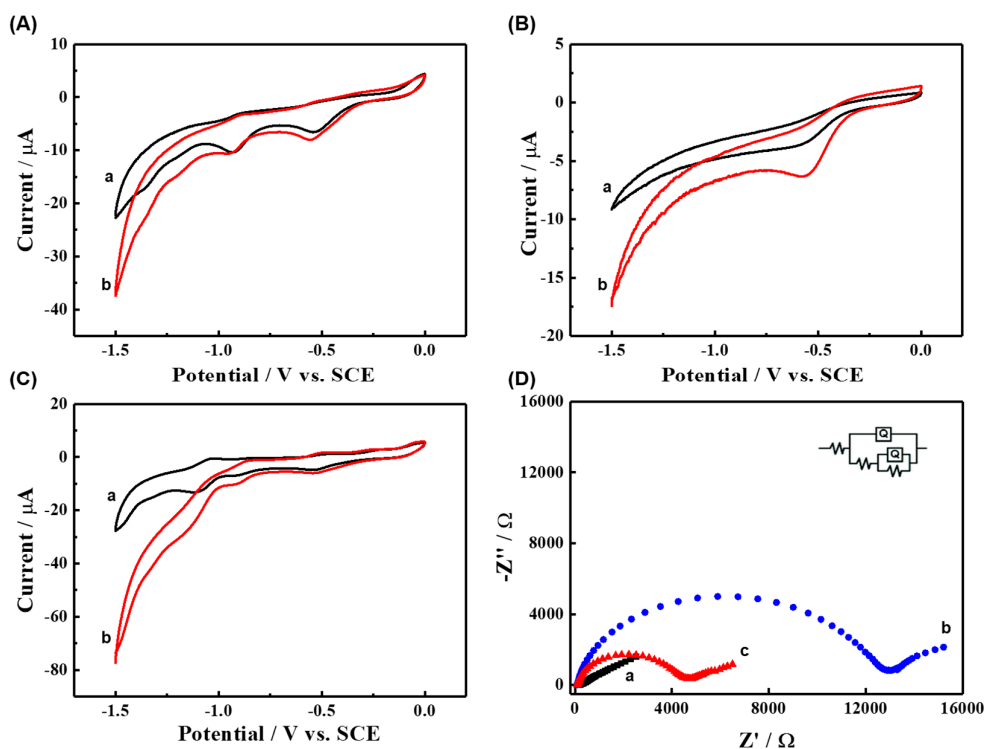
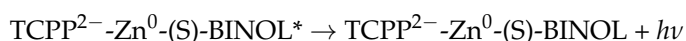
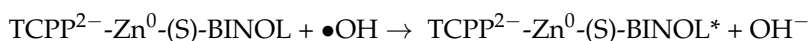
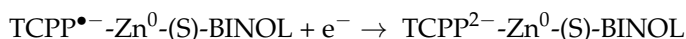
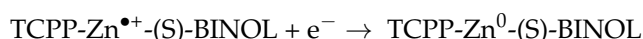
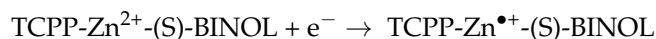
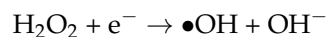


Figure 7. Cyclic voltammograms of (A) TCPP, (B) (S)-BINOL, and (C) TCPP-Zn-(S)-BINOL in 10 mM HEPES containing 0.3 M KCl in the absence (a) and presence (b) of 12 mM H_2O_2 . (D) Nyquist plots of bare GCE (a), TCPP/GCE (b), and TCPP-Zn-(S)-BINOL/GCE (c) in 0.1 M PBS containing 5.0 mM $[\text{Fe}(\text{CN})_6]^{4-/3-}$. The inset is the equivalent circuit.

Meanwhile, EIS measurements were performed on different modified electrodes in PBS buffer containing 5 mM $[\text{Fe}(\text{CN})_6]^{3-/4-}$ to further explain the mechanism of the enhanced ECL behavior of TCPP-Zn-(S)-BINOL/GCE. The impedance spectrum includes a linear part (representing a diffusion-limited process) and a semicircular part (representing an electron-transfer-limited process). The charge-transfer resistance (R_{ct}) is represented according to the diameter of the semicircle in the impedance spectra [37], which is related to the capability of electron transfer of a ferricyanide-redox probe between the electrolyte and the electrode. As shown, the R_{ct} of the bare electrode is 72Ω (Figure 7D, curve a). After modification of TCPP, the R_{ct} increases to $11,650 \Omega$ (Figure 7D, curve b), which indicates the

poor electron conductivity of TCPP. The R_{ct} of TCPP-Zn-(S)-BINOL/GCE (Figure 7D, curve c) is significantly lower than that of TCPP/GCE, indicating that the electron conductivity of the synthesized TCPP-Zn-(S)-BINOL is greatly improved.

Based on the experimental results, the possible ECL mechanism is proposed as the following response equations:



3.4. ECL Enantioselective Recognition of Tyr Enantiomers

The chiral recognition abilities of Tyr enantiomers were evaluated on TCPP-Zn-(S)-BINOL/GCE by an ECL method. The recognition efficiency was estimated by the ratio of ECL intensity ($\text{ECL}_L/\text{ECL}_D$). It can be seen from Figure 8 that the addition of D-Tyr will not cause significant changes in the ECL intensity of TCPP-Zn-(S)-BINOL/GCE. In the presence of L-Tyr, the ECL intensity increased from 4300 a.u. to 7000 a.u., and the recognition efficiency was 1.84. The phenomenon indicates that TCPP-Zn-(S)-BINOL/GCE prefers to recognize L-Tyr rather than D-Tyr, which may be attributed to the stronger hydrogen bond interaction between the (S)-BINOL in TCPP-Zn-(S)-BINOL and L-Tyr than D-Tyr. Therefore, L-Tyr is more easily attracted by the modified electrode of TCPP-Zn-(S)-BINOL.

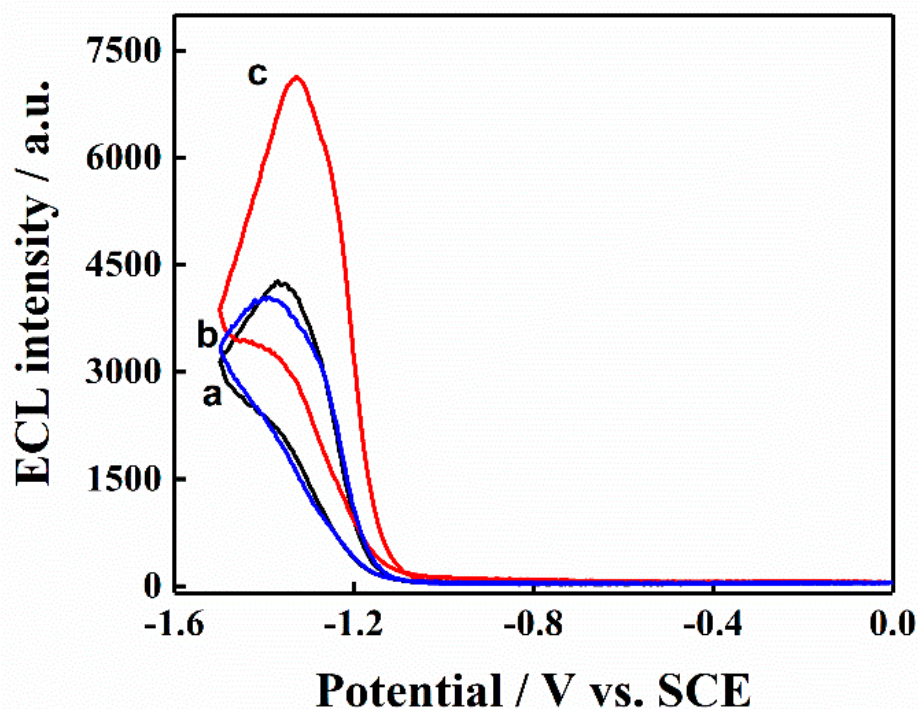


Figure 8. ECL potential curves of TCPP-Zn-(S)-BINOL/GCE in 10 mM HEPES containing 12 mM H_2O_2 before (a) and after the addition of 2 mM D-Tyr (b) and L-Tyr (c).

In order to verify this conjecture, EIS was measured before and after the incubation of TCPP-Zn-(S)-BINOL/GCE with Tyr enantiomers for 2 h in PBS buffers containing 5 mM $\text{Fe}(\text{CN})_6^{3-/4-}$. As shown in Figure 9A, the electron conductivity of the Tyr enantiomer is better than that of the prepared TCPP. From the results of Figure 9A, it can be seen that the R_{ct} value of D-Tyr/TCPP-Zn-(S)-BINOL/GCE is 4078 Ω , which has no significant change compared with the R_{ct} value of TCPP-Zn-(S)-BINOL/GCE (4294 Ω), while the R_{ct} value of L-Tyr/TCPP-Zn-(S)-BINOL/GCE is significantly decreased, which is 2006 Ω . This indicates that L-Tyr adsorbs to the electrode surface but D-Tyr does not. At the same time, the combination of L-Tyr and TCPP-Zn-(S)-BINOL improves the electron conductivity of the electrode, which is conducive to the amplification of the ECL signal.

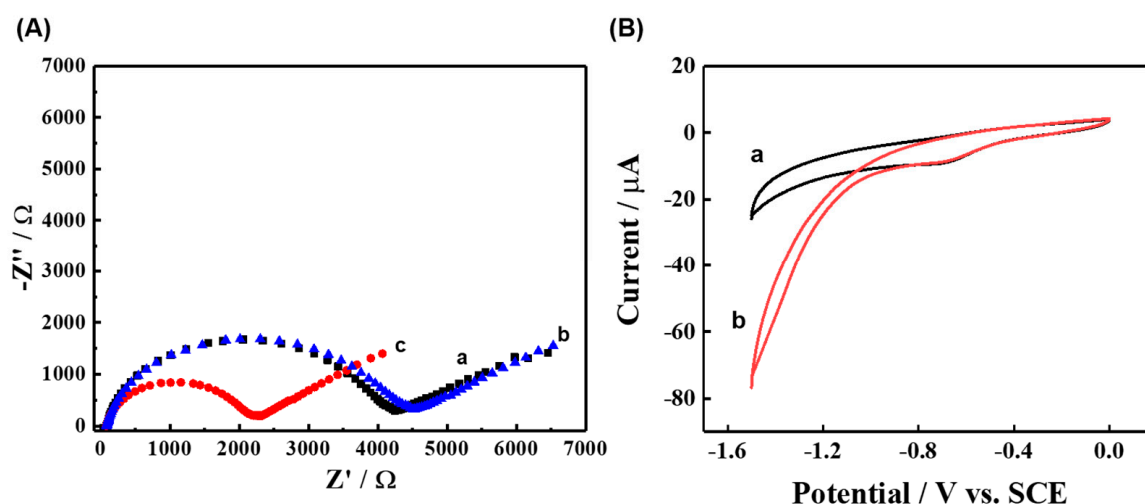
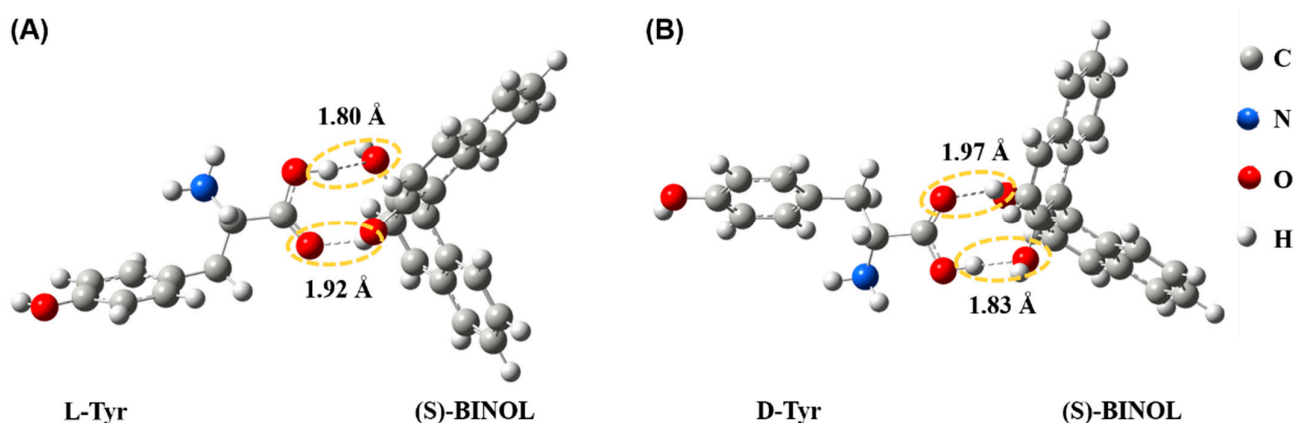


Figure 9. (A) Nyquist plots of TCPP-Zn-(S)-BINOL/GCE in 0.1 M PBS containing 5.0 mM $[\text{Fe}(\text{CN})_6]^{4-/3-}$ before (a) and after its incubation with 2 mM D-Tyr (b) and L-Tyr (c). (B) Cyclic voltammograms of L-Tyr/GCE in 0.1M HEPES containing 0.3 M KCl in the absence (a) and presence (b) of 12 mM H_2O_2 .

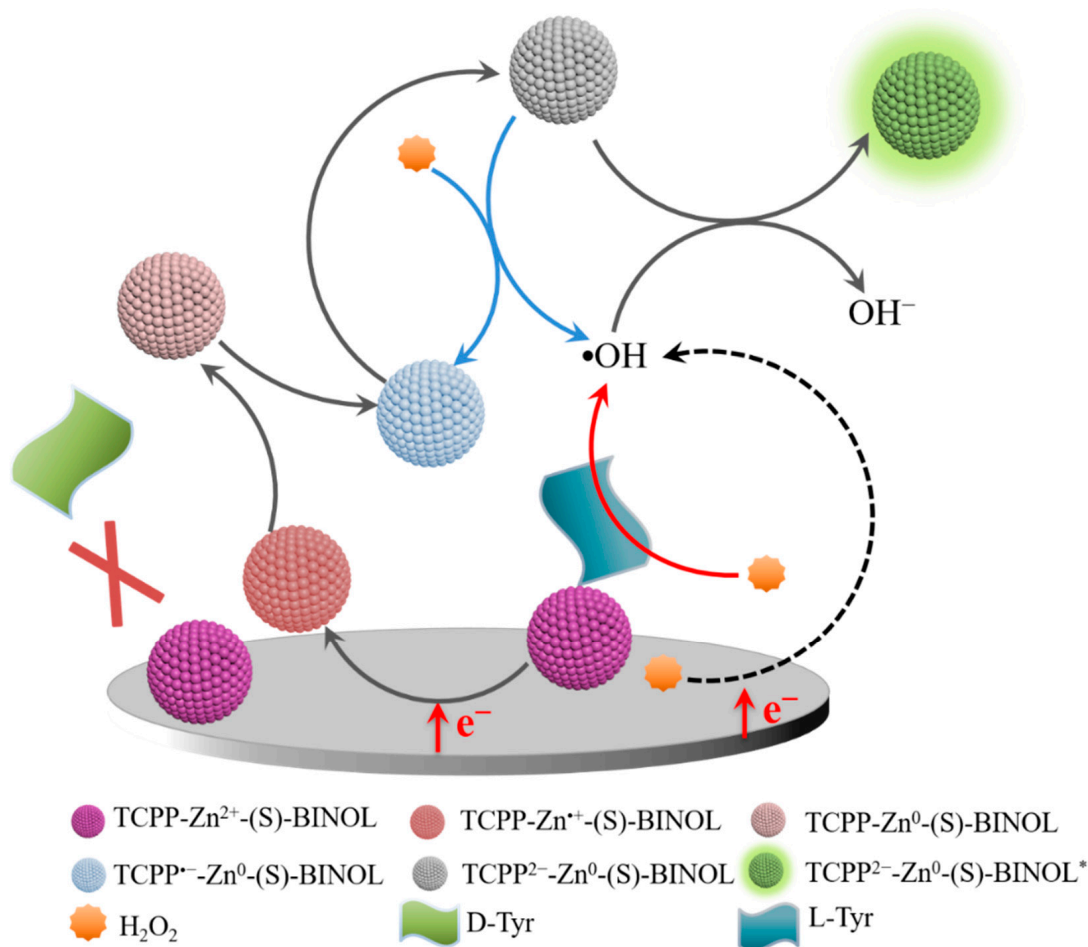
In addition, L-Tyr was also found to have a good catalytic reduction effect on hydrogen peroxide. It can be seen from Figure 9B that in the presence of H_2O_2 , the reduction current intensity of L-Tyr is significantly greater than that in the absence of H_2O_2 , indicating that L-Tyr can electrocatalytically reduce H_2O_2 to generate hydroxyl radicals, which is the key substance in ECL luminescence.

In order to further study the mechanism of chiral recognition, DFT was used to analyze the ground-state structures of different systems. For simplicity, (S)-BINOL was used in the MD simulation instead of TCPP-Zn-(S)-BINOL, because (S)-BINOL is the only chiral source in the module. Although (S)-BINOL can form two hydrogen bonds with L-Tyr (Scheme 3A) and D-Tyr (Scheme 3B), respectively, the bond length between (S)-BINOL and L-Tyr (1.80 \AA and 1.92 \AA) is slightly shorter than the corresponding bond length between (S)-BINOL and D-Tyr (1.83 \AA and 1.97 \AA). The short bond length indicates that (S)-BINOL is preferably combined with L-Tyr [38]. Therefore, TCPP-Zn-(S)-BINOL/GCE will preferentially combine with L-Tyr, and L-Tyr can electrocatalyze the reduction of H_2O_2 to generate hydroxyl radicals, which leads to an increase in ECL intensity.



Scheme 3. Optimized ground-state structures of the complexes of (A) (S)-BINOL + L-Tyr, (B) (S)-BINOL + D-Tyr.

Therefore, we speculate upon the ECL chiral recognition mechanism of Tyr enantiomers by TCPP-Zn-(S)-BINOL/GCE. As shown in Scheme 4, TCPP-Zn-(S)-BINOL/GCE selectively adsorbs L-Tyr, and the combination of L-Tyr improves the electron transport capacity of the electrode surface and helps the catalytic reduction of H_2O_2 to produce a large number of hydroxyl radicals. These two effects significantly increase the ECL intensity of TCPP-Zn-(S)-BINOL/GCE in the presence of L-Tyr, while D-Tyr will not combine with TCPP-Zn-(S)-BINOL on the electrode and will not change the ECL intensity of the electrode.



Scheme 4. Schematic illustration showing the mechanisms of ECL chiral recognition.

The ECL response of TCPP-Zn-(S)-BINOL/GCE to L-Tyr of different concentrations was investigated, as shown in Figure 10A. In the range of 0.1~2 mM, the ECL signal intensity of the electrochemical sensing platform increases significantly with the increase in L-Tyr concentration. As shown in Figure 10B, the linear regression equation can be expressed as $I = 8670.98 + 552.91 \lg C$ (I is the ECL intensity, C is the concentration of L-Tyr), the correlation coefficient $R^2 = 0.9927$, and the detection limit is 20 nM ($S/N = 3$). These results show that the ECL chiral sensor can be used as a chiral recognition platform as well as a chiral detection platform.

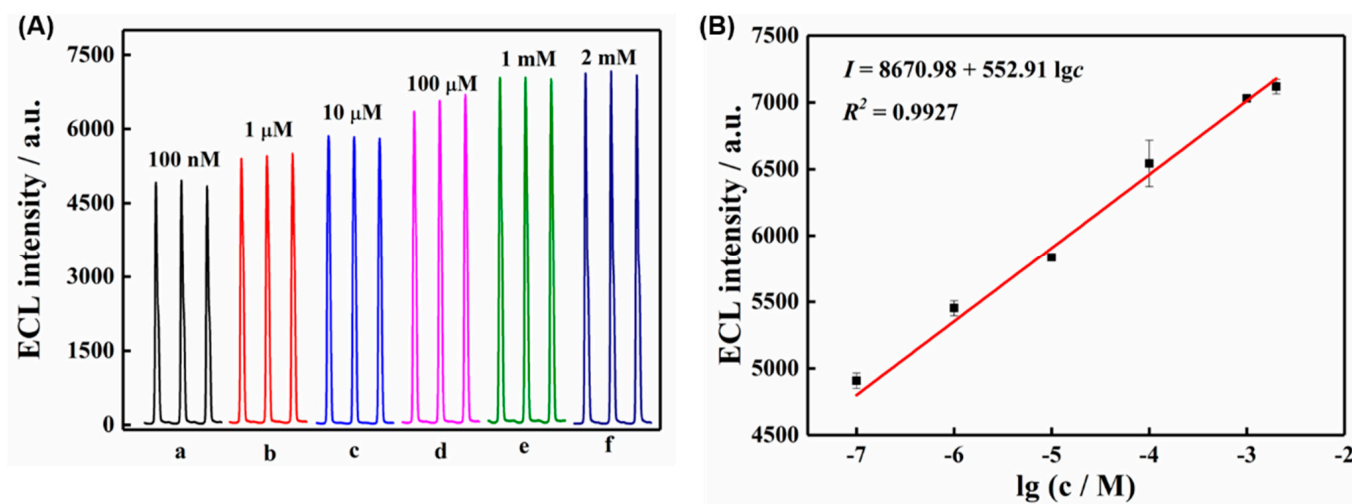


Figure 10. (A) ECL response of TCPP-Zn-(S)-BINOL/GCE to L-Tyr of different concentrations. (B) Linear relationship between ECL intensity and concentration of L-Tyr.

The selectivity of the proposed biosensor was studied by replacing the Tyr enantiomers with amino acid enantiomers with similar structures. The ECL behaviors of TCPP-Zn-(S)-BINOL/GCE in the presence of L/D-tryptophan, L/D-phenylalanine, L/D-arginine, L/D-proline, and L/D-histidine were studied. As shown in Figure 11, the ECL intensity did not change significantly after adding other amino acids to the electrolyte, which confirmed that the modified electrode has high selectivity for the chiral recognition of Tyr enantiomers.

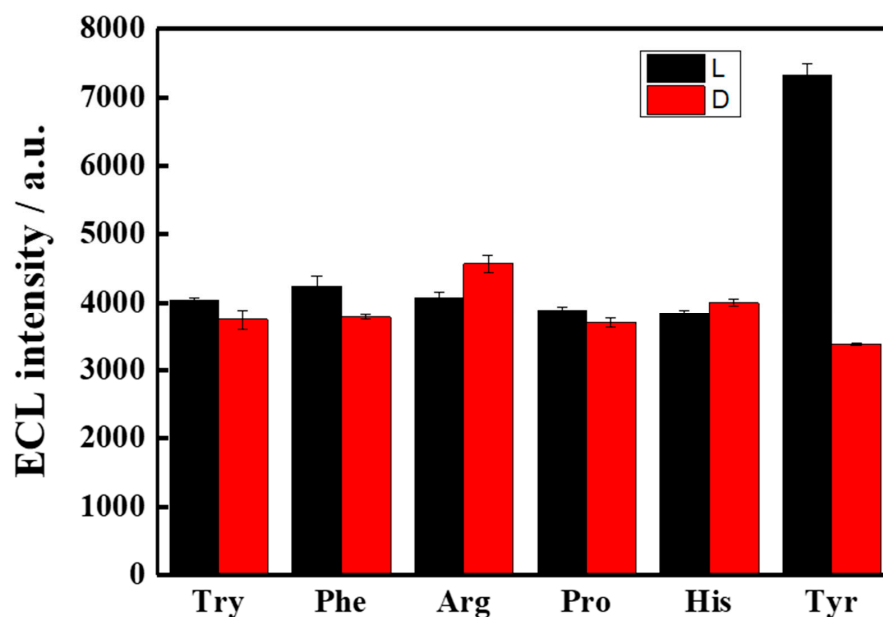


Figure 11. ECL responses for the discrimination of different amino acid enantiomers.

4. Conclusions

In this work, (S)-BINOL, as a chiral ligand, was assembled with a Zn-TCPP MOF to construct an efficient ECL chiral sensor. The preparation of porphyrin into an MOF structure can greatly improve its ECL luminescence efficiency, and the introduction of (S)-BINOL not only retains the enhanced ECL behavior of the porphyrin-based MOF but also imparts chirality to the material. The constructed chiral sensor based on TCPP-Zn-(S)-BINOL/GCE can selectively recognize Tyr enantiomers, and the recognition efficiency (ECL_L/ECL_D) can obtain 1.84. The recognition mechanism is verified by DFT, EIS, and CV results: the bond length between (S)-BINOL and L-Tyr is slightly shorter than the corresponding bond length between (S)-BINOL and D-Tyr; TCPP-Zn-(S)-BINOL/GCE can selectively adsorb L-Tyr, which can not only improve the electron transport capacity of the modified electrode surface but also help to catalyze hydrogen peroxide and generate a large number of hydroxyl radicals, resulting in an increase in ECL intensity. As a chiral sensor for detecting L-Tyr, TCPP-Zn-(S)-BINOL/GCE indicates a linear detection range of 100 nM to 2 mM, along with a detection limit of 20 nM ($S/N = 3$). These findings suggest that TCPP-Zn-(S)-BINOL may be a potential ECL chiral sensor, which is of great significance for pharmaceutical, medical, and life sciences.

Author Contributions: W.-R.C.: Conceptualization, investigation, writing—original draft preparation. W.-K.Z.: Data curation, methodology. B.-Z.Y.: Data curation. D.-T.W.: Data curation. J.-Y.L.: Resources. Z.-Z.Y.: Funding acquisition, writing—review and editing. Y.K.: Conceptualization, supervision, validation, writing—original draft preparation, project administration. All authors have read and agreed to the published version of the manuscript.

Funding: This research was funded by the Natural Science Foundation for Colleges and Universities in Jiangsu Province (no. 21KJB150018, 22KJB150018), the Science and Technology Program of Zhejiang Province (no. LGF22B050008), the Science and Technology Program of Jiaxing (no. 2022AY10012), and the Advanced Catalysis and Green Manufacturing Collaborative Innovation Center (no. ACGM2022-10-12).

Institutional Review Board Statement: Not applicable.

Informed Consent Statement: Not applicable.

Data Availability Statement: Not applicable.

Conflicts of Interest: The authors declare no conflict of interest.

References

1. Sanganyado, E.; Lu, Z.; Fu, Q.; Schlenk, D.; Gan, J. Chiral pharmaceuticals: A review on their environmental occurrence and fate processes. *Water Res.* **2017**, *124*, 527–542. [[CrossRef](#)] [[PubMed](#)]
2. Liang, R.P.; Liu, C.M.; Meng, X.Y.; Wang, J.W.; Qiu, J.D. A novel open-tubular capillary electrochromatography using β -cyclodextrin functionalized graphene oxide-magnetic nanocomposites as tunable stationary phase. *J. Chromatogr. A* **2012**, *1266*, 95–102. [[CrossRef](#)] [[PubMed](#)]
3. Zhu, G.; Kingsford, O.J.; Yi, Y.; Wong, K.Y. Recent advances in electrochemical chiral recognition. *J. Electrochem. Soc.* **2019**, *166*, H205. [[CrossRef](#)]
4. Zhao, Y.; Cui, L.; Ke, W.; Zheng, F.; Li, X. Electroactive Au@Ag nanoparticle assembly driven signal amplification for ultrasensitive chiral recognition of d-/l-Trp. *ACS Sustain. Chem. Eng.* **2019**, *7*, 5157–5166. [[CrossRef](#)]
5. Liu, H.; Shao, J.; Shi, L.; Ke, W.; Zheng, F.; Zhao, Y. Electroactive NPs and D-amino acids oxidase engineered electrochemical chiral sensor for D-alanine detection. *Sens. Actuators B* **2020**, *304*, 127333. [[CrossRef](#)]
6. Wu, S.; Ye, Q.; Wu, D.; Tao, Y.; Kong, Y. Enantioselective recognition of chiral tryptophan with achiral glycine through the strategy of chirality transfer. *Anal. Chem.* **2020**, *92*, 11927–11934. [[CrossRef](#)]
7. Myrgorodska, I.; Meinert, C.; Martins, Z.; le Sergeant d'Hendecourt, L.; Meierhenrich, U.J. Quantitative enantioseparation of amino acids by comprehensive two-dimensional gas chromatography applied to non-terrestrial samples. *J. Chromatogr. A* **2016**, *1433*, 131–136. [[CrossRef](#)]
8. Zhang, C.; Huang, W.X.; Chen, Z.; Rustum, A.M. Separation of chiral primary amino compounds by forming a sandwiched complex in reversed-phase high performance liquid chromatography. *J. Chromatogr. A* **2010**, *1217*, 4965–4970. [[CrossRef](#)]
9. Feizi, F.; Shamsipur, M.; Barati, A.; Gholivand, M.B.; Mousavi, F. Chiral recognition and quantitative analysis of tyrosine enantiomers using L-cysteine capped CdTe quantum dots: Circular dichroism, fluorescence, and theoretical calculation studies. *Microchem. J.* **2020**, *158*, 105168. [[CrossRef](#)]

10. Zhao, Q.; Wu, D.; Yin, Z.Z.; Cai, W.; Zhou, H.; Kong, Y. Fluorometric discrimination of tyrosine isomers based on the inner filter effect of chiral Au nanoparticles on MoS₂ quantum dots. *Anal. Methods* **2021**, *13*, 2290–2296. [[CrossRef](#)]
11. Wang, L.; Jin, Z.; Wang, X.; Zeng, S.; Sun, C.; Pan, Y. Pair of stereodynamic chiral benzylaldehyde probes for determination of absolute configuration of amino acid residues in peptides by mass spectrometry. *Anal. Chem.* **2017**, *89*, 11902–11907. [[CrossRef](#)]
12. Wang, L.; Chai, Y.; Ni, Z.; Wang, L.; Hu, R.; Pan, Y.; Sun, C. Qualitative and quantitative analysis of enantiomers by mass spectrometry: Application of a simple chiral chloride probe via rapid in-situ reaction. *Anal. Chim. Acta* **2014**, *809*, 104–108. [[CrossRef](#)]
13. Zhang, L.; Xu, C.; Liu, C.; Li, B. Visual chiral recognition of tryptophan enantiomers using unmodified gold nanoparticles as colorimetric probes. *Anal. Chim. Acta* **2014**, *809*, 123–127. [[CrossRef](#)]
14. Liu, C.; Lian, J.; Liu, Q.; Xu, C.; Li, B. β -Cyclodextrin-modified silver nanoparticles as colorimetric probes for the direct visual enantioselective recognition of aromatic α -amino acids. *Anal. Methods* **2016**, *8*, 5794–5800. [[CrossRef](#)]
15. Contino, A.; Maccarrone, G.; Remelli, M. Exploiting thermodynamic data to optimize the enantioseparation of underivatized amino acids in ligand exchange capillary electrophoresis. *Anal. Bioanal. Chem.* **2013**, *405*, 951–959. [[CrossRef](#)]
16. Wang, Y.; Yu, Z.; Ji, W.; Tanaka, Y.; Sui, H.; Zhao, B.; Ozaki, Y. Enantioselective discrimination of alcohols by hydrogen bonding: A SERS study. *Angew. Chem.* **2014**, *126*, 14086–14090. [[CrossRef](#)]
17. Sun, X.; Kong, H.; Zhou, Q.; Tsunega, S.; Liu, X.; Yang, H.; Jin, R.H. Chiral plasmonic nanoparticle assisted raman enantioselective recognition. *Anal. Chem.* **2020**, *92*, 8015–8020. [[CrossRef](#)]
18. Sun, X.; Wang, N.; He, Y.; Kong, H.; Yang, H.; Liu, X. Molecule-specific vibration-based chiral differentiation of Raman spectra using cysteine modified gold nanoparticles: The cases of tyrosine and phenylalanine. *J. Mater. Chem. B* **2021**, *9*, 7167–7171. [[CrossRef](#)]
19. Zhao, Q.; Yang, J.; Zhang, J.; Wu, D.; Tao, Y.; Kong, Y. Single-template molecularly imprinted chiral sensor for simultaneous recognition of alanine and tyrosine enantiomers. *Anal. Chem.* **2019**, *91*, 12546–12552. [[CrossRef](#)]
20. Hesari, M.; Ding, Z. A grand avenue to Au nanocluster electrochemiluminescence. *Acc. Chem. Res.* **2017**, *50*, 218–230. [[CrossRef](#)]
21. Zhao, G.; Wang, Y.; Li, X.; Yue, Q.; Dong, X.; Du, B.; Cao, W.; Wei, Q. Dual-quenching electrochemiluminescence strategy based on three-dimensional metal–organic frameworks for ultrasensitive detection of amyloid- β . *Anal. Chem.* **2019**, *91*, 1989–1996. [[CrossRef](#)] [[PubMed](#)]
22. Farinone, M.; Urbańska, K.; Pawlicki, M. BODIPY-and porphyrin-based sensors for recognition of amino acids and their derivatives. *Molecules* **2020**, *25*, 4523. [[CrossRef](#)] [[PubMed](#)]
23. Kameyama, K.; Morisue, M.; Satake, A.; Kobuke, Y. Highly Fluorescent Self-Coordinated Phthalocyanine Dimers. *Angew. Chem. Int. Ed.* **2005**, *44*, 4763–4766. [[CrossRef](#)] [[PubMed](#)]
24. Takeuchi, M.; Tanaka, S.; Shinkai, S. On the influence of porphyrin π – π stacking on supramolecular chirality created in the porphyrin-based twisted tape structure. *Chem. Commun.* **2005**, *44*, 5539–5541. [[CrossRef](#)] [[PubMed](#)]
25. Monti, D.; De Rossi, M.; Sorrenti, A.; Laguzzi, G.; Gatto, E.; Stefanelli, M.; Venanzi, M.; Luvidi, L.; Mancini, G.; Paolesse, R. Supramolecular Chirality in Solvent-Promoted Aggregation of Amphiphilic Porphyrin Derivatives: Kinetic Studies and Comparison between Solution Behavior and Solid-State Morphology by AFM Topography. *Chem. Eur. J.* **2020**, *16*, 860–870. [[CrossRef](#)]
26. Weyandt, E.; Filot, I.A.; Vantomme, G.; Meijer, E. Consequences of amide connectivity in the supramolecular polymerization of porphyrins: Spectroscopic observations rationalized by theoretical modelling. *Chem. Eur. J.* **2021**, *27*, 9700–9707. [[CrossRef](#)]
27. Kari, N.; Zannotti, M.; Giovannetti, R.; Řeha, D.; Minofar, B.; Abliz, S.; Yimit, A. Metallic Effects on p-Hydroxyphenyl Porphyrin Thin-Film-Based Planar Optical Waveguide Gas Sensor: Experimental and Computational Studies. *Nanomaterials* **2022**, *12*, 944. [[CrossRef](#)]
28. Qiao, X.; Arsalan, M.; Ma, X.; Wang, Y.; Yang, S.; Wang, Y.; Sheng, Q.; Yue, T. A hybrid of ultrathin metal-organic framework sheet and ultrasmall copper nanoparticles for detection of hydrogen peroxide with enhanced activity. *Anal. Bioanal. Chem.* **2021**, *413*, 839–851. [[CrossRef](#)]
29. Zhang, C.; Han, M.; Yu, L.; Qu, L.; Li, Z. Fabrication an electrochemical sensor based on composite of Cu-TCPP nanosheets and PSS functionalized graphene for simultaneous and sensitive determination of dihydroxybenzene isomers. *J. Electroanal. Chem.* **2021**, *890*, 115232. [[CrossRef](#)]
30. Hang, L.; Zhang, T.; Wen, H.; Liang, L.; Li, W.; Ma, X.; Jiang, G. Controllable photodynamic performance via an acidic microenvironment based on two-dimensional metal-organic frameworks for photodynamic therapy. *Nano Res.* **2021**, *14*, 660–666. [[CrossRef](#)]
31. Tu, W.; Lei, J.; Wang, P.; Ju, H. Photoelectrochemistry of Free-Base-Porphyrin-Functionalized Zinc Oxide Nanoparticles and Their Applications in Biosensing. *Chem. Eur. J.* **2011**, *17*, 9440–9447. [[CrossRef](#)]
32. Ibrahim, M.N.M.; Zakaria, N.; Sipaut, C.S.; Sulaiman, O.; Hashim, R. Chemical and thermal properties of lignins from oil palm biomass as a substitute for phenol in a phenol formaldehyde resin production. *Carbohydr. Polym.* **2011**, *86*, 112–119. [[CrossRef](#)]
33. Zhao, M.; Wang, Y.; Ma, Q.; Huang, Y.; Zhang, X.; Ping, J.; Zhang, Z.; Lu, Q.; Yu, Y.; Xu, H.; et al. Ultrathin 2D metal–organic framework nanosheets. *Adv. Mater.* **2015**, *27*, 7372–7378. [[CrossRef](#)]
34. Xiao, Y.; Guo, W.; Chen, H.; Li, H.; Xu, X.; Wu, P.; Shen, Y.; Zheng, B.; Huo, F.; Wei, W.D. Ultrathin 2D Cu-porphyrin MOF nanosheets as a heterogeneous catalyst for styrene oxidation. *Mater. Chem. Front.* **2019**, *3*, 1580–1585. [[CrossRef](#)]

35. Cai, W.R.; Zeng, H.B.; Xue, H.G.; Marks, S.R.; Cosnier, S.; Zhang, X.J.; Shan, D. Enhanced Electrochemiluminescence of Porphyrin-Based Metal–Organic Frameworks Controlled via Coordination Modulation. *Anal. Chem.* **2019**, *92*, 1916–1924. [[CrossRef](#)]
36. Zhang, G.Y.; Deng, S.Y.; Zhang, X.J.; Shan, D. Cathodic electrochemiluminescence of singlet oxygen induced by the electroactive zinc porphyrin in aqueous media. *Electrochim. Acta* **2016**, *190*, 64–68. [[CrossRef](#)]
37. Xiao, J.; Hu, X.; Wang, K.; Zou, Y.; Gyimah, E.; Yakubu, S.; Zhang, Z. A novel signal amplification strategy based on the competitive reaction between 2D Cu-TCPP (Fe) and polyethyleneimine (PEI) in the application of an enzyme-free and ultrasensitive electrochemical immunosensor for sulfonamide detection. *Biosens. Bioelectron.* **2020**, *150*, 111883. [[CrossRef](#)]
38. Ye, Q.; Guo, L.; Wu, D.; Yang, B.; Tao, Y.; Deng, L.; Kong, Y. Covalent functionalization of bovine serum albumin with graphene quantum dots for stereospecific molecular recognition. *Anal. Chem.* **2019**, *91*, 11864–11871. [[CrossRef](#)]